Mechanism and experimental study on the photocatalytic performance of Ag/AgCl @ chiral TiO_2 nanofibers photocatalyst: the impacts of wastewater components

Dawei Wang [a], Yi Li[a]*, Gianluca Li Puma[b], Chao Wang [a], Peifang Wang [a], Wenlong Zhang [a] and Qing Wang [a]

[a] *Key Laboratory of Integrated Regulation and Resource Development of Shallow Lakes, Ministry of Education, College of Environment, Hohai University. Xi Kang Road #1, Nanjing 210098, PR China; E-mail: envly@hhu.edu.cn*

[b] *Environmental Nanocatalysis & Photoreaction Engineering, Department of Chemical Engineering, Loughborough University, Loughborough LE11 3TU, United Kingdom.*

Abstract

The effects of secondary effluent components on the photocatalytic performances of Ag/AgCl @ chiral TiO_2 nanofibers and the undergoing mechanisms were investigated. These effects were evaluated through the water components-induced changes on the net rate of HO· generation and modeled using a relative rate technique. Dissolved organic matter DOM (k = -2.8×10^8 $M^{-1}s^{-1}$) scavenged reactive oxygen species, Cl^- (k = -5.3×10^8 $M^{-1}s^{-1}$) accelerated the transformation from Ag to AgCl (which is not photocatalytic active under visible-light irradiation), while Ca^{2+} (c>50 mM) (k = -1.3×10^9 $M^{-1}s^{-1}$) induced aggregation of Ag/AgCl and thus all of them reveled inhibitory effects. NO_3^- (k = 6.9×10^8 $M^{-1}s^{-1}$) and CO_3^{2-} (k = 3.7×10^8 $M^{-1}s^{-1}$) improved the photocatalytic ability of Ag/AgCl slightly by improving the rate of HO· generation. Other ubiquitous secondary effluent components including SO_4^{2-} (k = 3.9×10^5 $M^{-1}s^{-1}$), NH_3^+ (k = 3.5×10^5 $M^{-1}s^{-1}$) and Na^+ (k = 2.6×10^4 $M^{-1}s^{-1}$) had negligible effects. 90% of EE2 spiked in the secondary effluent was removed within 12 min, while the structure and size of Ag/AgCl @ chiral TiO_2 nanofibers remained stable. This work may be helpful not only to uncover the photocatalytic mechanism of Ag/AgCl based photocatalyst but also to elucidate the transformation and transportation of Ag and AgCl in natural water.

Key Words: *wastewater components, Ag, AgCl, photocatalytic performance, transformation*

1. Introduction

The irradiation of photocatalytic semiconductor materials with photons of wavelength equal or less than their bandgap, results in the formation of electron-hole couples which promote reduction and oxidation reactions. This unique property of semiconductors has been used to develop environmental remediation technologies in wastewater treatment, air purification, bacteria disinfection and surface self-cleaning [1-3]. Even though studies on photocatalysis have progressed steadily, the wide-scale commercial application of this technology is slowly starting. Two of the most important issues are (i) the reduction of the effective photocatalytic efficiency due to the competing electron-hole recombination process and (ii) the unsatisfactory visible-light response [4,5]. Some high-performance wide-gap photocatalysts such as TiO_2 and ZnO can only absorb UV light (wavelength < 400 nm), making them unattractive regarding the use of the full spectrum of solar light [6]. Numerous attempts have been made to overcome the above mentioned fundamental and technological barriers which are necessary to widen the practical range of applications of semiconductor photocatalysis. Among these, the coupling of Ag and AgCl compounds (abbreviated as Ag/AgCl below) at the nanoscale has attracted significant attention due to its unique plasmonic property and high photocatalytic performance under visible-light irradiation [7-9]. In our early communication we have shown that, Ag/AgCl immobilized on chiral TiO_2 nanofibers (Ag/AgCl @ chiral TiO_2 nanofibers) is a highly active and stable photocatalyst in the aqueous environment [10]. In such configuration, the surface plasmon resonance of Ag is accelerated by the chiral

nanostructure of the TiO_2 nanofibers, which can tune the polarization of the incident light, resulting in an enhanced photocatalytic response of Ag/AgCl. Powerful reactive oxygen species (ROS) are generated with visible light irradiation, which can oxidize organic pollutants [11-13]. However, the application of such new photoactive material for the removal of contaminants in wastewater and drinking water needs to be demonstrated. This is of significance as (i) the influence of water matrix components on the generation of ROS is complex and will finally affect the photocatalytic performance of Ag/AgCl [14-16], and (ii) Ag nanoparticles (AgNPs) and silver ions (Ag^+) which may be released into the wastewater and drinking water can potentially induce antibacterial and antiviral impacts [17]. Preliminary studies have been conducted to understand the impacts of different water components on the dissolution, transformation and transportation of AgNPs. For example, the dissolved organic matter (DOM) in the water might lead to its adsorption on AgNPs [18], and hence reducing the environmental and ecological risk. Mg^{2+} may also promote the aggregation of AgNPs by screening the electrostatic double layer repulsion between like-charged particles, thereby decreasing silver dissolution [19]. The effects of wastewater components on the photocatalytic performance and stability of Ag/AgCl are undiscovered, while AgCl is less photoactive and more stable due to its lower solubility, and the interplay between AgCl and Ag will significantly change the properties of Ag/AgCl.

The objective of this study is to derive new insight into the photocatalytic degradation of emerging contaminants such as 17-β-ethynylestradiol (EE2) by Ag/AgCl @ chiral

TiO_2 nanofibers in "actual water effluents" from an urban water treatment plant and to evaluate the impacts of ubiquitous secondary effluent components such as DOM, Na^+, Ca^{2+}, NH_3^+, NO_3^-, SO_4^{2-}, CO_3^{2-} and Cl^- on the photocatalytic performance and nanostructure stability of the Ag/AgCl @ chiral TiO_2 nanofibers. To the best of our knowledge, this is the first report on the photocatalytic performace of Ag/AgCl based nanomaterial in the real wastewaters. This work may be helpful to elucidate the photocatalytic mechanism of Ag/AgCl based nanomaterials and may also help unravel the transport of silver in aqueous media.

2. Experimental section

2.1 Reagents

17-β-ethynylestradiol (EE2) (analytical grade) was obtained from Merck. The salts (Na_2CO_3, $NaHCO_3$, Na_2SO_4, $(NH_4)_2SO_4$, $Ca(NO_3)_2$) used in synthetic water were analytical grade and purchased from Sigma-Aldrich. Pony lake fulvic acid (PLFC) was obtained from the International Humic Substance Society. All solutions were prepared with distilled water which was further processed through an 18 MΩ/cm Milli-Q cm water purification system. Details of the synthesis and characterization of Ag/AgCl @ chiral TiO_2 nanofibers visible-light photocatalyst, which was selected as representative of Ag/AgCl based nanomaterials, are reported in our previous study[10]. Ag/AgCl@ chiral TiO_2 nanofiers with different Ag contents were obtained through varying the photoreduction time. We synthesized Ag/AgCl nanoparticles using a similar recipe with that in ref 5. Simply, Ag_2MoO_4 was firstly synthesized by

mixing $AgNO_3$ and Na_2MoO_4 solutions under pH=8.0. The mixture was heated at 180□ for 1h and led to precipitation of Ag_2MoO_4. AgCl was obtained by the ion-exchange reaction between Ag_2MoO_4 and HCl. Then, the obtained AgCl was dispersed in methanol solutions and irradiated by Xe arc lamp (with an ultraviolet cutoff filter to provide visible light with wavelength larger than 400 nm). The products was washed and dried in air.

2.2 Photocatalytic degradation

The photocatalytic degradation experiments of EE2 was performed with the powder photocatalyst (0.1 g) suspended in an aqueous solution (100 mL) of EE2 (5 mg/L). The light source was a 300W Xe arc lamp (Philips) with a UV cut-off filter (providing visible light $\lambda \geq 400$ nm). The irradiation experiments were carried out in a 500 ml beaker placed under the light (12cm, with stirring). The depth of liquid was 3 cm (see Fig S1). Each irradiation experiment started after an equilibration time of 30 min in the dark to establish adsorption/desorption equilibrium of EE2 over the catalyst.

2.3 Analytical methods

The concentrations of EE2 in aqueous samples were determined by high performance liquid chromatography (HPLC, Agilent 1100) analysis with a DB-624 capillary column (30m×0.32mm×1.80μm). Mobile phase of 70% methanol (Merck) and 30% water, flow rate of 0.5 mL/min, injection volume of 10μL, and absorption wavelength of 280 nm.

Inorganic ions were quantified using ion chromatography (IC, Waters 2690, USA)

coupled with an IC-PAK anion HR column (4.6 mm×75 mm, Waters, USA) and a 432 conductivity detector (Waters, USA). The eluent was a solution of NaOH (30 mmol/L) flowing at a flow rate of 1.2 mL/min. DOM was measured on selected samples by means of a Shimadzu TOC-V_{CPN} fitted with an ANSI-V autosampler. The kinetics of HO· formation was investigated by nanosecond laser flash photolysis technique [20]. Photocatalysts samples (new and used) were filtered, dried at 60℃ and then used analyzed by transmission electron microscopy (TEM), X-ray diffraction (XRD) and UV-vis spectroscopy. TEM was performed on a JEOL 2011 operation at 200 kV. XRD patterns were recorded on a Rigaku X-ray diffractometer D/MAX-2200/PC equipped with Cu *Kα* radiation (40 kV, 20 mA). UV-vis diffuse reflectance spectroscopy was performed in triplicate on similar samples to ensure reproducibility, on a SHIMADZU UV-2450 with a collection speed of 40 nm min^{-1} and $BaSO_4$ as the reference.

2.4 Evaluation of kinetic rates

The impacts of the water matrix components on the photocatalytic degradation of EE2 were evaluated through the rate of HO· formation. The second-order rate constants for the reactions between HO· and water components were determined by a relative rate technique proposed in our previous study [20]. Firstly, carbonate was added into the suspension of Ag/AgCl @ chiral TiO_2 nanofibers, EE2 and distilled water to estimate the rate of HO· formation from the irradiated Ag/AgCl @ chiral TiO_2 nanofibers:

$$\mathrm{Ag/AgCl@chiralTiO_2} \xrightarrow{light} \cdot\mathrm{OH} \qquad k_0 \qquad (3)$$

$$\cdot OH + CO_3^{2-} \rightarrow CO_3^{\cdot-} + OH^- \qquad k_1 = 3.7\times10^8\ M^{-1}s^{-1} \qquad (4)$$

$$\cdot OH + HCO_3^- \rightarrow CO_3^{\cdot-} + H_2O \qquad k_2 = 8.5\times10^6\ M^{-1}s^{-1} \qquad (5)$$

$$EE2 + \cdot OH \rightarrow CO_2 + H_2O \qquad k_3 = 9.8\times10^9\ M^{-1}s^{-1} \qquad (6)$$

The mole balance on ·OH in the batch reactor is:

$$\frac{d[\cdot OH]}{dt} = k_0[\text{Ag/AgCl@chiralTiO}_2] - (k_1[CO_3^{2-}] - k_2[HCO_3^-] - k_3[EE2])[\cdot OH] \qquad (7)$$

The concentration of ·OH as a function of time (t) after the laser pulse:

$$[\cdot OH]_t = k_0[\text{Ag/AgCl@chiralTiO}_2]t + [\cdot OH]_0 e^{-(k_1[CO_3^{2-}]+k_2[HCO_3^-]+k_3[EE2])t} \qquad (8)$$

Similarly, the formation of $CO_3^{\cdot-}$ as s function of time is:

$$[CO_3^{\cdot-}]_t = \frac{(k_1[CO_3^{2-}] + k_2[HCO_3^-])[\cdot OH]_0(1 - k_0[\text{Ag/AgCl@chiralTiO}_2]t - e^{-(k_0[\text{Ag/AgCl@chiralTiO}_2]-k_1[CO_3^{2-}]-k_2[HCO_3^-]-k_3[EE2])t})}{k_1[CO_3^{2-}] + k_2[HCO_3^-] + k_3[EE2] - k_0[\text{Ag/AgCl@chiralTiO}_2]} \qquad (9)$$

Taking into consideration the molar absorption extinction coefficient, the transient absorbance of $CO_3^{\cdot-}$ at 600 nm at time t could be expressed as

$$A_t(CO_3^{\cdot-}) = \varepsilon(CO_3^{\cdot-}) \cdot l \cdot [CO_3^{\cdot-}]_t \qquad (10)$$

where $\varepsilon(CO_3^{\cdot-})$ is the molar absorption extinction coefficient of $CO_3^{\cdot-}$ at 600 nm and l is the optical path length.

The absorbance of $CO_3^{\cdot-}$ at 600 nm after a laser pulse can be determined from:

$$A_f(CO_3^{\cdot-}) = \frac{\varepsilon(CO_3^{\cdot-}) \cdot l \cdot (k_1[CO_3^{2-}] + k_2[HCO_3^-])[\cdot OH]_0(-k_0[\text{Ag/AgCl@chiralTiO}_2]t)}{k_1[CO_3^{2-}] + k_2[HCO_3^-] + k_3[EE2] - k_0[\text{Ag/AgCl@chiralTiO}_2]} \qquad (11)$$

The rate of ·OH formation can be derived by varying the ($CO_3^{2-} + HCO_3^-$) concentration (C). In these experiments, the concentration of ($CO_3^{2-} + HCO_3^-$) was

varied in the range from 0.1 to 0.8 mmol, at fixed pH of 7.5 and EE2 concentration of 1.26 mg/L.

In the absence of EE2 in the solution the absorbance of $CO_3^{\cdot-}$ at 600 nm is:

$$A_f(CO_3^{\cdot-})_{[EE2]=0} = \frac{\varepsilon(CO_3^{\cdot-})\cdot l\cdot(k_1[CO_3^{2-}]+k_2[HCO_3^-])[\cdot OH]_0}{k_1[CO_3^{2-}]+k_2[HCO_3^-]-k_0[Ag/AgCl@chiralTiO_2]} \quad (12)$$

Equation (12) divided by (11) gives:

$$A_f(CO_3^{\cdot-})_{[EE2]=0} = \frac{\varepsilon(CO_3^{\cdot-})\cdot l\cdot(k_1[CO_3^{2-}]+k_2[HCO_3^-])[\cdot OH]_0(-k_0[Ag/AgCl@chiralTiO_2]t)}{k_1[CO_3^{2-}]+k_2[HCO_3^-]-k_0[Ag/AgCl@chiralTiO_2]} \quad (13)$$

Since the pH was 7.5, the concentration of CO_3^{2-} and HCO_3^- was calculated from following two equations according to the dissociation equilibrium, respectively:

$$[CO_3^{2-}] = \frac{k_{a1}(H_2CO_3)k_{a2}(H_2CO_3)C}{k_{a1}(H_2CO_3)[H^+]+k_{a1}(H_2CO_3)k_{a2}(H_2CO_3)} = 0.01C \quad (14)$$

$$[HCO_3^-] = C-[CO_3^{2-}] = 0.99C \quad (15)$$

Where C=[CO_3^{2-}]+[HCO_3^-] , $k_{a1}(H_2CO_3)$ is the first dissociation constant of H_2CO_3 equal to 4.2×10^{-7}, and $k_{a2}(H_2CO_3)$ is the second dissociation constant of H_2CO_3 equal to 5.6×10^{-11} [21]. Substitution of k_1, k_2 and k_3 in equation (13) yields:

$$\frac{A_f(CO_3^{\cdot-})_{[EE2]=0}}{A_f(CO_3^{\cdot-})} = 1+\frac{1.4\times10^6}{1.2\times10^7 C-k_0[Ag/AgCl@chiralTiO_2]} \quad (16)$$

From equation (16), k_0 was estimated to be $(5.2\pm0.1)\times10^7\,g^{-1}s^{-1}$ (the kinetic rate was calculated using the weight of Ag/AgCl @ chiral TiO_2 nanofibers as its molecular weight cannot be determined) by weighed least-square fit of the plot of $A_f(CO_3^{\cdot-})_{[EE2]=0}/A_f(CO_3^{\cdot-})$ against C (Fig. S2). Similarly, the rate constants of the

reactions between HO· and the other water components were estimated (Table 1, and supporting information for further details).

3. Results and Discussion

3.1 Photocatalytic mechanism of Ag/AgCl @ chiral TiO_2 nanofibers

The SEM results showed the chiral nanostructures were obtained after the synthesis. (Fig. S3). The chiral TiO_2 nanofibers were loaded with different Ag contents by varing the photoreduction time (Table S1). The TEM and XRD results confirmed the synthesis of Ag/AgCl nanoparticles (Fig. S4). Different photocatalytic abilities of the tested photocatalysts were observed (Fig. S5). The mechanism of photocatalytic performance of Ag/AgCl @ chiral TiO_2 nanofibers has been reported in our previous study [10]. The excitation of surface plasmon resonance of Ag is caused by the irradiation with sunlight and polarized light rotated by the chiral structure. Then two simultaneous photo-processes occur. A strong electronic coupling between Ag and AgCl conduction bands, which injects photoinduced electrons in the Ag NPs quickly and efficiently into the AgCl and TiO_2, yielding superoxide radicals, and finally HO· radicals from the reductive pathway. The other process involves holes which transfer to the surface of Ag (since the surface of AgCl is negatively charged and most likely terminated by Cl^- ions due to light induced reduction of Ag^+ ions). The transferred holes oxidize Cl^- to Cl^0, rapidly regenerating Ag, stabilizing the Ag/AgCl immobilized onto chiral TiO_2 nanofibers.

To elucidate the roles of the ROS responsible for the degradation of EE2 over

Ag/AgCl @ chiral TiO_2 nanofibers, methanol, $NaHCO_3$ and *p*-benzoquinone were used to quench $HO\cdot$, h^+ and $\cdot O_2^-$, respectively (Fig. 1). The rate of photocatalytic degradation of EE2 exhibited a slight variation in the presence of $NaHCO_3$, but a contrast test indicated that this was due to an increase of pH [22], implying that h^+ have negligible contribution on the degradation of EE2. *p*-benzoquinone quencher had almost no influence on the photocatalytic degradation of EE2, indicating no $\cdot O_2^-$ existed in the solution. In consequence, it can be concluded that $HO\cdot$ plays a key role in the photocatalytic degradation of EE2. This result is consistent with above mentioned photocatalytic mechanism of Ag/AgCl @ chiral TiO_2 nanofibers since all of h^+ and Cl^0 can undergo a series of reactions and produce $HO\cdot$ [23,24]:

$$h^+ + OH^- \rightarrow \cdot OH \quad (17)$$

$$Cl^0 + OH^- \rightarrow Cl^- + \cdot OH \quad (18)$$

3.2 Effect of water matrix components on the photocatalytic activity of Ag/AgCl @ chiral TiO_2 nanofibers

The photocatalytic activity and stability of Ag/AgCl @ chiral TiO_2 nanofibers in wastewater can be attributed to a series of complex reactions among Ag^0, Ag^+, Cl^-, ROS and their corresponding products[10]. All of them should be taken into account to elucidate the effects of water matrix components on the photocatalytic performance of Ag/AgCl @ chiral TiO_2 nanofibers.

3.2.1 Effect of DOM

DOM here represented by fulvic acid is a heterogeneous mixture of organic

compounds excreted by microorganisms and break-down products from decomposing organisms ubiquitous in natural water [25]. The results in Fig. 2 revealed that the presence of DOM in the water inhibited the photocatalytic degradation of EE2 over Ag/AgCl @ chiral TiO_2 nanofibers, and that the inhibitory effects become more obvious with the increasing of the DOM concentrations. This may be attributed to the ROS scavenging ability of the DOM as we demonstrated in our previous study [20]. However, such mechanism may further be influenced by (i) the possibility that DOM may adsorb onto the Ag nanoparticles (AgNPs) [26] which can further prevent the generation of electron-hole pairs and disable the photocatalytic ability of Ag/AgCl @ chiral TiO_2 nanofibers and (ii) by aggregation of nanoparticles induced by DOM [27] which can further decrease the photocatalytic activity of this catalyst. Herein, TEM, FT-IR and zeta potential (Fig. 3) were carried out to unravel the inhibitory mechanism of DOM. TEM pictures (Fig. 3a and 3b) of Ag/AgCl @ chiral TiO_2 nanofibers in the absence and in the presence of DOM did not show obvious differences, suggesting that the DOM adsorption and coating on the catalyst may not be the cause of concern. This supports the hypothesis that the observed inhibitory effect of DOM on the photocatalytic degradation of EE2 should be due to the ROS scavenging. The absence of clear differences in the stretching vibrations of CH, CO, C=C and COO^- bonds in the FT-IR spectra (Fig. 3c) of Ag/AgCl @ chiral TiO_2 nanofibers in the absence and in the presence of DOM also supports this mechanism.

The TEM and FT-IR results also demonstrate the stability of Ag/AgCl @ chiral TiO_2 nanofibers in the presence of DOM, which further suggests that DOM does not

interfere with the cyclic transformation of Ag and AgCl under irradiation. This conclusion is thermodynamically sound, as the redox potential for fulvic acid ~0.5 V (*vs.* NHE), is not sufficient to overcome the highly negative redox potential of Ag^{+} to Ag^{0} (-1.8 V *vs.* NHE) [28]. Furthermore, the zeta potential results (Fig. 3d) indicated that the inhibitory effect of DOM cannot be attributed to the aggregation of photocatalytic particle in suspension.

3.2.2. Effect of anions

The impact of anions on the photocatalytic degradation of EE2 by Ag/AgCl @ chiral TiO_2 nanofibers was investigated using sodium salts which can avoid the potential simultaneous effects of cations. In these salts, Na^{+} is at its maximum oxidation state therefore it will not compete as hole scavenger [20]. Furthermore, Na^{+} at concentrations less than 100 mM does not influence the charge at the surface of the catalyst and does not promote the agglomeration of AgNPs [25]. Cl^{-} inhibited the photocatalytic degradation of EE2 significantly and the rate of inhibition increased with the concentrations of Cl^{-} in solution (Fig. 4). In contrast, the SO_4^{2-} did not influence the degradation rates, while NO_3^{-} and CO_3^{2-} anions were found to accelerate the rates of photocatalytic degradation of EE2 slightly(Fig. 4).

The inhibition by chloride anions has been attributed to the preferential displacement of the catalyst surface bound $HO\cdot$ by Cl^{-} in previous studies [20, 27]. However, such displacement should result in the oxidization from Cl^{-} to Cl^{0} (the most reactive species toward one-electron oxidation [28]) according to the photocatalytic

mechanism of Ag/AgCl @ chiral TiO_2 nanofibers, the result of which would be an acceleration of the photocatalytic ability of Ag/AgCl @ chiral TiO_2 nanofibers. This apparent incongruity was resolved by UV-vis spectroscopy and XRD analysis of the photocatalysts exposed to Cl^- solutions.

The absorption spectra of pristine Ag/AgCl @ chiral TiO_2 nanofibers at 200-350 nm can be attributed to the characteristic absorption of the AgCl semiconductor [29] and of TiO_2, while the response in the visible-light region (400-800 nm) results from the creation of surface plasmon resonance [30] (Fig. 5a). This red-shift compared with pure Ag nanoparticles may be attributed to the high dielectric constant of the semiconductors in the neighborhood. In the presence of chloride, the shift of the main absorbance peak to higher wavelengths in the ultraviolet region corresponds to an increase of the average size of the AgCl nanoparticles, while the weakening of the plasmon peak in the visible region implies a decrease of Ag content in the photocatalyst. These UV-vis spectra differences of Ag/AgCl @ chiral TiO_2 nanofibers in the presence and in the absence of chloride point towards to the transformation of the immobilized Ag within the photocatalyst into AgCl in the presence of Cl^-, a conclusion that was further evidenced by the observed XRD patterns (Fig. 5b) of the two samples. The peak (at ~27°) corresponding to AgCl strengthened, indicating an increase of the size of AgCl crystals. Furthermore, the weaken peak of Ag (at ~46°) indicated that the size of Ag decreased after exposed to chloride. Therefore, the oversupply of Cl^- in solution initiates the transformation from Ag to AgCl, which dulls the visible-light photocatalytic activity of Ag/AgCl @ chiral TiO_2 nanofibers.

The XRD patterns of Ag/AgCl @ chiral TiO_2 nanofibers in the presence and in the absence of SO_4^{2-}, CO_3^{2-} and NO_3^- did not show significant differences (Fig. S6), implying few changes on size and structure of this nanomaterial. This can be attributed to that dissolved Ag^+ ions which generated from photocatalytic process of Ag/AgCl @ chiral TiO_2 nanofibers, are less soluble as AgCl than Ag_2SO_4, $AgNO_3$ and Ag_2CO_3[19]. Therefore, it can be concluded that AgCl prevents Ag from reacting with inorganic ligands and thus stabilizes the Ag/AgCl system. However, the slight photocatalytic accelerations of NO_3^- and CO_3^{2-} were observed, due to their ability to generate HO· (photolysis of NO_3^- and CO_3^{2-} is an inevitable source of HO·) [31], while they did not induce any aggregation or dissolution.

3.2.3. Effect of cations

The impact of NH_4^+ on the photocatalytic activity of Ag/AgCl @ chiral TiO_2 nanofibers was investigated using the SO_4^{2-} which only exhibited a negligible influence on the photocatalytic degradation performance of this photocatalyst as discussed above. However, $Ca(NO_3)_2$ was chosen not $CaSO_4$ to investigate the effect of Ca^{2+} as $CaSO_4$ is sparingly soluble and will limit the concentration variations of Ca^{2+}. It was found that $Ca(NO_3)_2$ with c< 50 mM can improve the photocatalytic ability while it inhibited the performances when its concentration is > 50 mM (Fig. 6a). Detailed comparison showed that the slight improvement fitted the character of NO_3^- (Fig. 4c). The comparison between TEM pictures of pristine Ag/AgCl @ chiral TiO_2 nanofibers (Fig. 3a) and of the sample exposed to 100 mM $Ca(NO_3)_2$ (Fig. 6b)

revealed that Ca^{2+} induced aggregation of the photocatalyst particles which would further inhibit its photocatalytic activity. The compression of the electrical double layer at a high ionic strength ($c(Ca^{2+}) > 50$ mM) resulted in this particle aggregation and precipitation [32, 33]. Due to its divalent nature, the screening of Ag and AgCl charges by Ca^{2+} is significant, which hence contrasts with the negligible impact of Na^{+} describe above [33]. No distinct influence of NH_4^{+} on the photocatalytic performance of Ag/AgCl @ chiral TiO_2 nanofibers (Fig. S7) was observed, which is also consistent with the previous findings [18, 34].

3.3 Photocatalytic degradation of EE2 in an actual urban wastewater effluent

The photocatalytic degradation of EE2 spiked in a secondary effluent from an urban wastewater treatment plant over Ag/AgCl @ chiral TiO_2 nanofibers was investigated. The water characteristics (Table 2) show the presence of both anions and cations in the effluent. The conversion of EE2 under visible light irradiation (90% in 12 min) was found to be marginally less than the conversion of EE2 determined in synthetic water (~ 86% in 12 min) (Fig 7a). The difference should be ascribed to the ROS scavenging ability of the DOM as discussed in the above section. The XRD results of the pristine catalyst and the catalyst after the removal of EE2 in the effluent (Fig. 7b) were found to be identical, indicating that Cl^{-} and Ca^{2+} at such low concentrations in the wastewater did not influence the degradation of EE2. Meanwhile, the TOC of the wastewater was partially photocatalytic degraded (from 13 mg/L to 8 mg/L). The above results showed that Ag/AgCl @ chiral TiO_2 nanofibers remained highly active

and stable even in an actual secondary wastewater effluent, for the removal of an emerging contaminant such as EE2.

The photocatalytic degradation of EE2 over Ag/AgCl @ chiral TiO_2 nanofibers in the secondary effluent was also simulated using the kinetic model described in Section 2.4, including the evaluation of the relative rate constants. The pseudo-first order kinetic equation describing the degradation of EE2 in deionized water is [35]

$$[\mathrm{EE2}]_t = [\mathrm{EE2}]_0 e^{-kt} \qquad (19)$$

where k is the pseudo-first order kinetic constant (k was estimated to be 4.46×10^{-3} s^{-1} from Fig 7a). When EE2 and Ag/AgCl @ chiral TiO_2 nanofibers were exposed to the actual secondary wastewater effluent, the kinetic constant decreased by a factor α:

$$[\mathrm{EE2}]_t = [\mathrm{EE2}]_0 e^{-\alpha kt} \qquad (20)$$

$$\text{where } \alpha = \frac{(k_0[\mathrm{Ag/AgCl@chiralTiO_2}] - k_a[\mathrm{SO_4^{2-}}] - k_b[\mathrm{CO_3^{2-}}] - \cdots\cdots k_c[\mathrm{EE2}])}{k_c[\mathrm{EE2}]} \qquad (21)$$

The relative kinetic rate constants of the water components (Table 1) were substituted into equation (20) and (21) to simulate the EE2 photocatalytic degradation over Ag/AgCl @ chiral TiO_2 nanofibers (Fig. 7a). Considering the entire set of experimental conditions employed, a root square lower than 5.35% (calculated from equation 22) was obtained, indicating a satisfactory agreement between the model and experimental results [36].

$$\mathrm{error}(\%) = \sum_{i=1}^{n}\left(\frac{C_{\mathrm{mod}} - C_{\mathrm{exp}}}{C_{\mathrm{exp}}}\right)^2 \qquad (22)$$

4. Conclusion

The results indicate that Na^+, NH_4^+, SO_4^{2-} which are all ubiquitous components in natural water have no influence on the stability and photoactivity of Ag/AgCl compound, although Cl^- could initiate the transformation from Ag to AgCl, and Ca^{2+} could induce the aggregation of nanomaterials containing Ag. DOM in the water inhibited the photocatalytic activity of Ag/AgCl based nanomaterial but had no influence on its size and morphology. NO_3^- and CO_3^{2-} promoted the generation of ROS. It can be concluded that, Ag nanoparticles in natural water in the presence of Cl^- could stabilize and form Ag/AgCl compound which prevents the release of Ag^+ ion into natural water. This effect may be useful to explain the transformation of Ag nanoparticles and its potential risk to environment. The results suggest that Ag/AgCl based nanomaterials are active and stable in a secondary effluent from an actual wastewater treatment plant. Further advances in the development of advanced Ag/AgCl photocatalysts may results in further increases in photocatalytic activity for the removal of emerging contaminants in water and for its successful implementation in domestic and industrial wastewater treatment processes.

Acknowledgement

The study was financially supported by the National Natural Science Foundation of China (No. 51322901), and the Fundamental Research Funds for the Central Universities (No. 2014B02914) and the research fund provided by the National Basic Research Program of China ('973' program, No. 2010CB429006).

Reference

[1] Hoffmann, M.R., Martin, S.T., Choi, W., Bahnemannt, D.W., 1995. Environmental applications of semiconductor photocatalysis. Chemical Review. 95, 69-96.

[2] Li Puma, G., Khor, J.N., Brucato A., 2004. Modeling of an annular photocatalytic reactor for water purification: oxidation of pesticides. Environmental Science and Technology. 38, 3737-3745.

[3] Salvadó-Estivill, I., Hargreaves, D.M., Li Puma, G., 2007. Evaluation of the intrinsic photocatalytic oxidation kinetics of indoor air pollutants. Environmental Science and Technology. 41, 2028-2035.

[4] Puddu, V., Mokaya, R., Li Puma, G., 2007. Novel one step hydrothermal synthesis of TiO_2/WO_3 nanocomposites with enhanced photocatalytic activity. Chemical Communications. 45, 4749-4751.

[5] Wang, P., Huang, B., Qin, X., Zhang, X., Dai, Y., Wei, J., Whangbo, M-H., Ag@AgCl: A Highly Efficient and Stable Photocatalyst Active under Visible Light. Angew. Chem. Int. Ed. 2008, 47, 7931-7933

[6] Zhang, X., Chen, Y.L., Liu, R-S and Tsai, D. P., 2013. Plasmonic photocatalysis.

Reports on Progress in Physics. 76 (4), 046401.

[7] Fang, Z., Zhu, X., 2013. Plasmonic in nanostructures. Advanced Materials. 25, 3840-3856.

[8] Odom, T.W., Schatz, G.Z., 2011. Introduction to plasmonic. Chemical Reviews. 111, 3667-3668.

[9] Brongersma, M.L., Shalaev, V.M., 2010. The case for plasmonic. Science. 328, 440-441.

[10] Wang, D., Li, Y., Li Puma, G., Wang, C., Wang, P., Zhang, W., Wang, Q., 2013. Ag/AgCl@helical chiral TiO_2 nanofibers as a visible-light driven plasmon photocatalyst. Chemical Communication. 47, 10367-10369.

[11] Brus, L., 2008. Nobel metal nanocrystals: plasmon electron transfer photochemistry and single-molecule Raman spectroscopy. Accounts of Chemical Research. 41, 1742-1749.

[12] Burda, C., Chen, X., Narayanan, R., El-Sayed, M.A., 2005. Chemistry and properties of nanocrystals of different shapes. Chemical reviews. 105, 1025-1102.

[13] Hu, C., Yu, J.C., Hao, Z., Wong, P.K., 2003. Effects of acidity and inorganic ions on the photocatalytic degradation of different azo dyes. Applied catalysis B: Environmental. 46, 35-47.

[14] Mckay, G., Dong, M.M., Kleinman, J.L., Mezyk, S.P., Rosario-Ortiz, F.L., 2011. Temperature dependence of the reaction between the hydroxyl radical and organic matter. Environmental Science and Technology. 45, 6932-6937.

[15] Huang, L., Li, L., Dong, W., Liu, Y., Hou, H., 2008. Removal of ammonia by

OH radical in aqueous phase. Environmental Science and Technology. 42, 8070-8075.

[16] Akaighe, N., MacCuspie, R.I., Navarro, D.A., Aga, D.S., Banerjee, S., Sohn, M., Sharma, V.K., 2011. Humic acid-induced silver nanoparticle formation under environmentally relevant conditions. Environmental Science and Technology. 45, 3895-3901.

[17] Navarro, E., Piccapietra, F., Wagner, B., Marconi, F., Kaegi, R., Odzak, N., Sigg, L., Behra, R., 2008. Toxicity of silver nanoparticles to Chlamydomonas reinhardtii. Environmental Science and Technology. 42, 8959-8964.

[18] Jin, X., Li, M., Wang, J., Marambio-Jones, C., Peng, F., Huang, X., Damoiseaux, R., Hoek, E.M.V., 2010. High-throughput screening of silver nanparticles stability and bacterial inactivation in aquatic media: influence of specific ions. Environmental Science and Technology. 44, 7321-7328.

[19] Cushing, S. K., J. Meng, Li, F., Senty, T. R., Suri, S., Zhi, M., Li, M., Bristow, A. D. and Wu, N., 2012. Photocatalytic activity enhanced by plasmonic resonant energy transfer from metal to semiconductor. Journal of the American Chemical Society. 134, 15033-15041.

[20] Wang, D., Li, Y., Li, G., Wang, C., Zhang, W., Wang, Q., 2013. Modeling of quantitative effects of water components on the photocatalytic degradation of 17α-ethynylestradiol in a modified flat plate serpentine reactor. Journal of Hazardous Materials. 254-255, 64-71.

[21] Dong, R., Tian, B., Zeng, C., Li, T., Wang, T., Zhang, J., 2013. Ecofriendly synthesis and photocatalytic activity of uniform cubic Ag@AgCl plasmonic

photocatalyst. Journal of Physical Chemistry C. 117, 213-220.

[22] Hu, C., Peng, T.W., Hu, X.X., Nie, Y.L., Zhou, X.F., Qu, J.H., He, H., 2010. Journal of the American Chemical Society. 132, 857-862.

[23] Zhou, X.F., Hu, C., Hu, X.X., Peng, T.W., Qu, J.H., 2010. The Journal of Physical Chemistry C. 114, 2746-2750

[24] Chen, L., Tang, X., Shen C., Chen C., Chen Y., 2012. Photosensitized degradation of 2 4', 5-trichlorobiphenyl (PCB 31) by dissolved organic matter. Journal of Hazardous Materials. 201-202, 1-6.

[25] Piccapietra, F., Sigg, L., Behra, R., 2012. Colloidal stability of carbonate-coated silver nanoparticles in synthetic and natural freshwater. Environmental Science and Technology. 46, 818-825.

[26] Gentry, S.T., Fredericks, S.J., Krchnavek, R., 2009. Controlled particle growth of silver sols through the use of hydroquinone as a selective reducing agent. Langmuir. 25, 2613-2621.

[27] Chong, M.N., Jin, B., Chow, C.W.K., Saint, C., 2010. Recent development in photocatalytic water treatment technology: a review. Water Research. 44, 2997-3027.

[28] Park, H., Vecitis, C.D., Hoffmann, M.R., 2009. Electrochemical water splitting coupled with organic compound oxidation: the role of active chlorine species. The Journal of Physical Chemistry. 113, 7935-7945.

[29] Wang, P., Huang, B., Lou, Z., Zhang, X., Qin, X., Dai, Y., Zheng, Z., Wang, X., 2010. Synthesis of highly efficient Ag@AgCl plasmonic photocatalysts with various structures. Chemistry: A European Journal. 16, 538-544.

[30] Shen, X., Song, C., Wang, J., Shi, D., Wang, Z., Liu, N., Ding, B., 2012. Rolling Up Gold Nanoparticle-Dressed DNA Origami into Three-Dimensional Plasmonic Chiral Nanostructures. Journal of the American Chemical Society. 134, 146-149.

[31] Wang, K., Zhang, J.Y., Lou, L.P., Yang, S.Y., Chen, Y.X., 2004. UV or visible light induced photodegradation of AO7 on TiO_2 particles: the influence of inorganic anions. Journal of Photochemistry and Photobiology A: Chemistry. 165, 201-207.

[32] Delay, M., Dolt, T., Woellhaf, A., Sembritzki, R., Frimmel, F.H., 2011. Interactions and stability of silver nanoparticles in the aqueous phase: influence of natural organic matter (NOM) and ionic strength. Journal of Chromatography A. 1218, 4206-4212.

[33] Thio, B.J., Montes, M.O., Mahmoud, M.A., Lee, D.W., Zhou, D., Keller, A.A., 2012. Mobility of capped silver nanoparticles under environmentally relevant conditions. Environmental Science and Technology. 46, 6985-6991

[34] Mumper, C.K., Ostermeyer, A., Semprini, L., Radniecki, T.S., 2013. Influence of ammonia on silver nanoparticle dissolution and toxicity to Nitrosomonas europaea. Chemosphere. 93, 2493-2498.

[35] Huang, L., Dong, W., Hou, H., 2007. Investigation of the reactivity of hydrated electron toward perfluorinated carboxylates by laser flash photolysis. Chemical Physics Letters. 436, 124-128.

[36] Lian, C., Wang, L., Chen, X., Han, X., Zhao, S., Liu, H., Hu, Y., 2014. Modeling Swelling Behavior of Thermoresponsive Polymer Brush with Lattice Density Functional Theory. Langmuir 30, 4040−4048

Tables

Table. 1. The derived relative second-rate rate constants

Water components	Relative values of kinetic rate constants ($M^{-1}s^{-1}$)[a]
DOM	-2.8×10^{8}
Cl^-	-5.3×10^{8}
SO_4^{2-}	3.9×10^{5}
CO_3^{2-}	Not determined
NO_3^-	6.9×10^{8}
Ca^{2+}	-1.3×10^{9}
Na^+	2.6×10^{4}
NH_3^+	3.5×10^{5}

[a] The water component can accelerate the HO· generation if its relative value>0.

Table. 2. The effluent characteristics of the municipal wastewater treatment plant in Suzhou, China.

Parameters	Values
TOC	13 mg/L
NO_3^-	1.2 mM
NH_4^+	3.2 mM
Cl^-	2.5 mM
SO_4^{2-}	0.3 mM
CO_3^{2-}	0.6 mM
Na^+	0.2 mM
Ca^{2+}	0.6 mM

Figure Captions

Fig. 1. Photocatalytic degradation curves of EE2 over Ag/AgCl @ chiral TiO_2 nanofibers under (**a**) no scavenger, (**b**) 10 mM methanol, (**c**) 0.1 M methanol, (**d**) 6 mM $NaHCO_3$ (pH=10.0), (**e**) NaOH solution (pH=10.0), (**f**) 0.1 mM *p*-benzoquinone.

Fig. 2. Effect of DOM on the photocatalytic degradation of EE2

Fig. 3. Effect of DOM on Ag/AgCl @ chiral TiO_2 nanofibers. (**a**) TEM picture of pristine Ag/AgCl @ chiral TiO_2 nanofibers, (**b**) TEM picture of Ag/AgCl @ chiral TiO_2 nanofibers after photocatalytic degradation of EE2 (exposure in 50 mM DOM), (**c**) FT-IR spectra of pristine Ag/AgCl @ chiral TiO_2 nanofibers (black trace) and Ag/AgCl @ chiral TiO_2 nanofibers after exposure to DOM solutions (red trace), (**d**) zeta potential of Ag/AgCl @ chiral TiO_2 nanofibers exposed to EE2 solutions with 50 mM DOM for different time. Scale bars in (**a**) and (**b**) represent 30 and 50 nm, respectively.

Fig. 4. The effect of (**a**) Cl^-, (**b**) SO_4^{2-}, (**c**) NO_3^- and (**d**) CO_3^{2-} on the photocatalytic degradation of EE2

Fig. 5. UV-vis diffuse reflectance spectra (**a**) and XRD patterns (**b**) of pristine Ag/AgCl @ chiral TiO_2 nanofibers and Ag/AgCl @ chiral TiO_2 nanofibers after exposure to 100 mM Cl^- solution.

Fig. 6. (**a**) The effect of Ca^{2+} on the photocatalytic performances of Ag/AgCl @ chiral TiO_2 nanofibers. (**b**) TEM picture of Ag/AgCl @ chiral TiO_2 nanofibers exposed to 100 mM $Ca(NO_3)_2$. Scale bar in (**b**) represents 50 nm.

Fig. 7. (**a**) Photocatalytic performances and kinetic simulations of Ag/AgCl @ chiral TiO_2 nanofibers in EE2 (dissolved in deionized water and secondary effluent) solution. (**b**) XRD patterns of pristine Ag/AgCl @ chiral TiO_2 nanofibers and exposed to secondary effluent.

Figures

Fig. 1

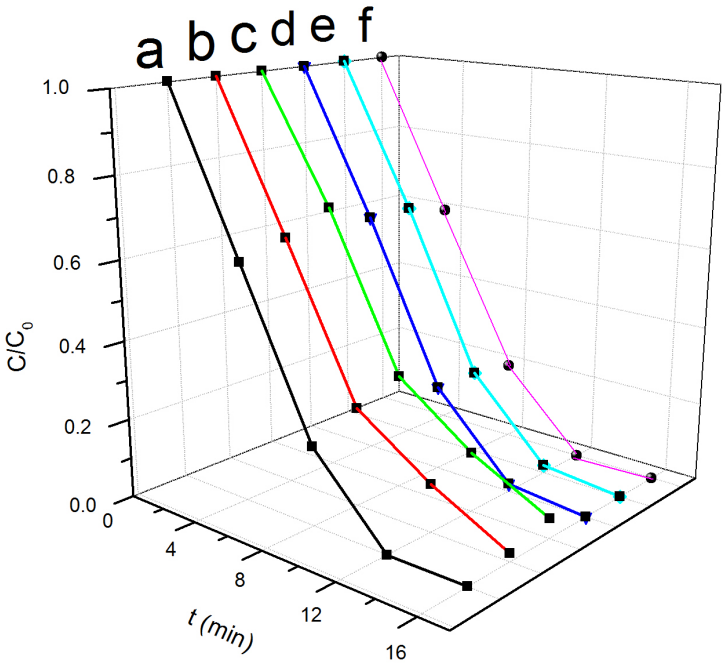

Fig. 2

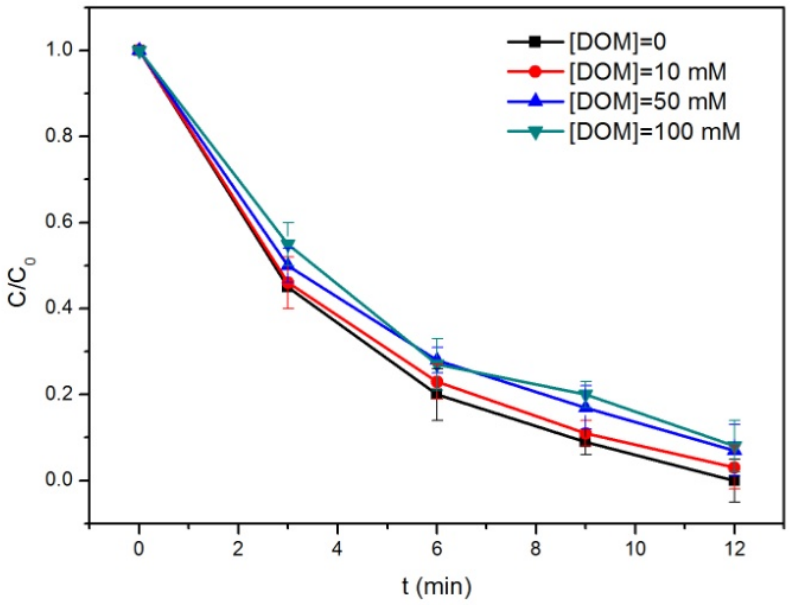
[DOM]=0
[DOM]=10 mM
[DOM]=50 mM
[DOM]=100 mM
C/C0
t (min)
0.0
0.2
0.4
0.6
0.8
1.0
0
2
4
6
8
10
12

Fig. 3

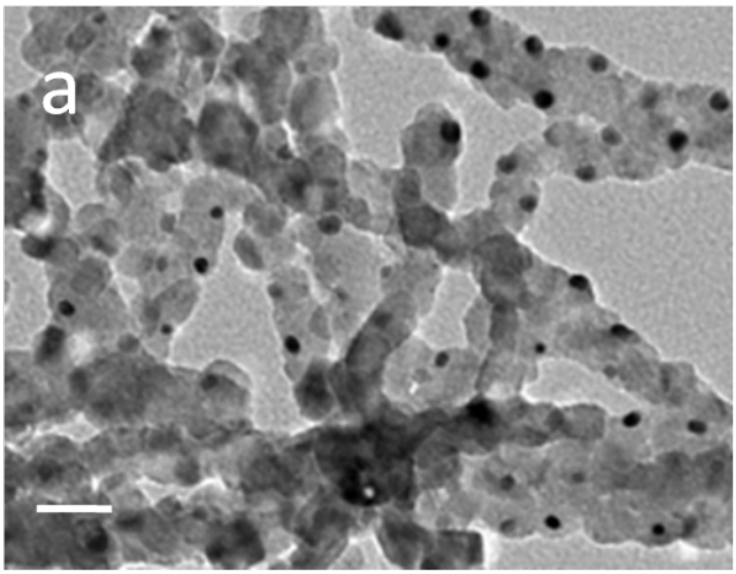

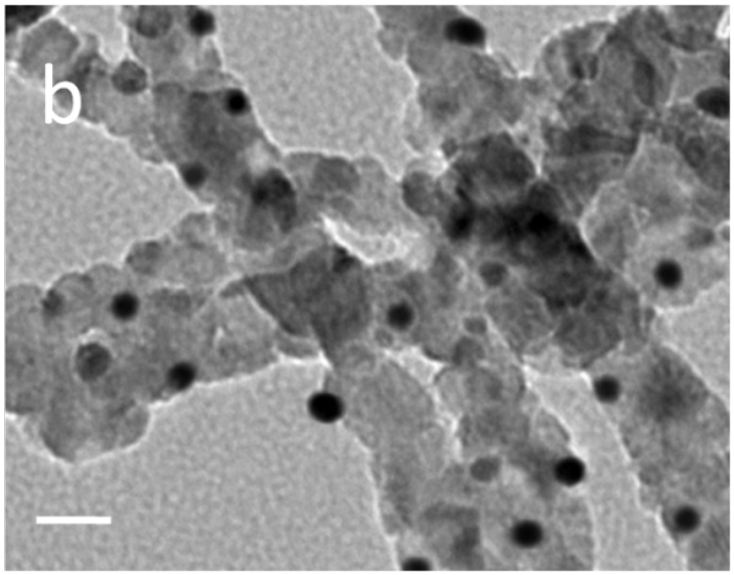

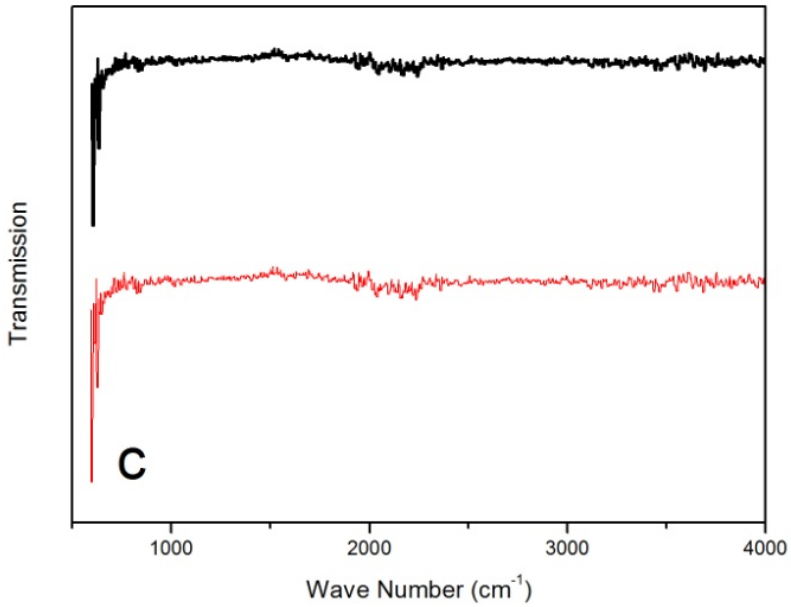
Transmission
c
1000
2000
3000
4000
Wave Number (cm-1)

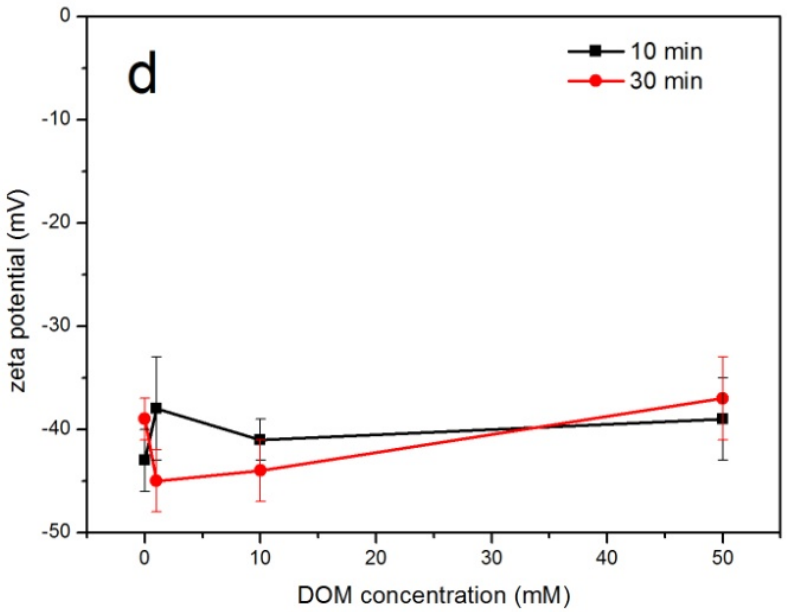
d
10 min
30 min
zeta potential (mV)
0
-10
-20
-30
-40
-50
0
10
20
30
40
50
DOM concentration (mM)

Fig. 4.

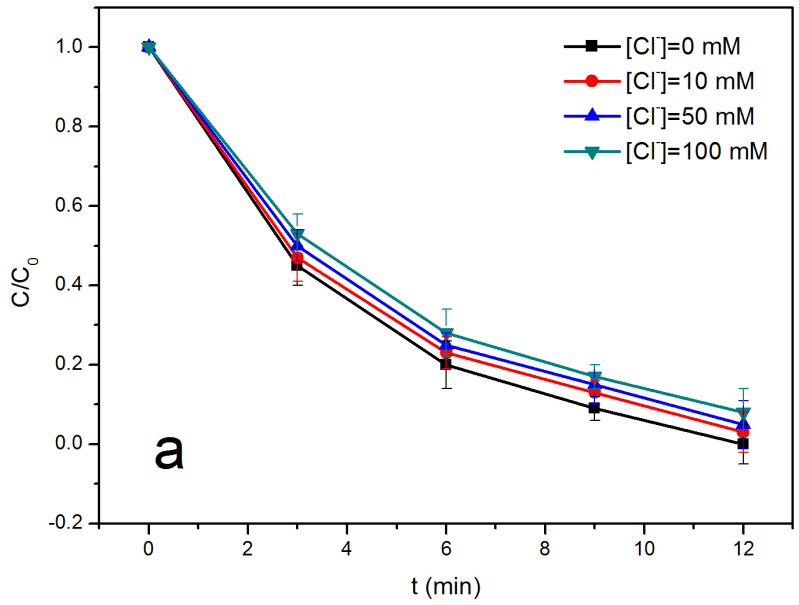
[Cl⁻]=0 mM
[Cl⁻]=10 mM
[Cl⁻]=50 mM
[Cl⁻]=100 mM
a
C/C0
t (min)

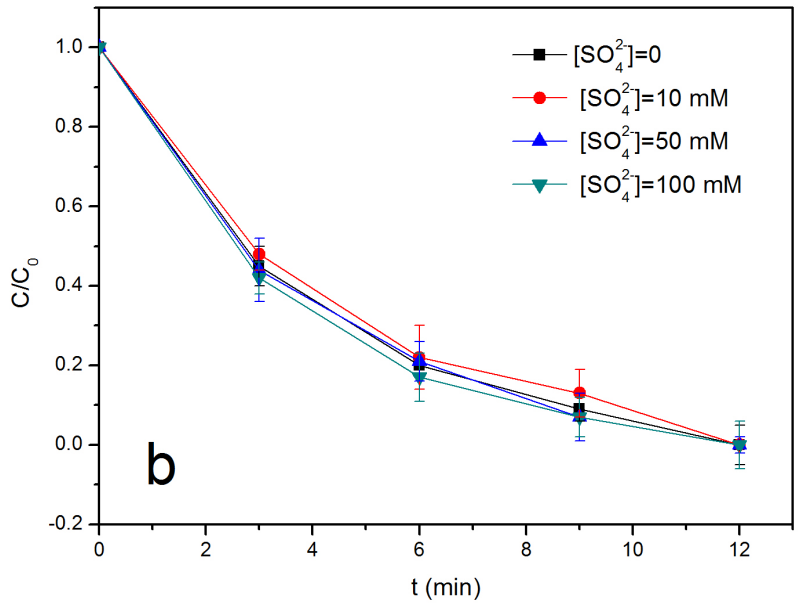
[SO4 2-]=0
[SO4 2-]=10 mM
[SO4 2-]=50 mM
[SO4 2-]=100 mM
b
C/C0
t (min)

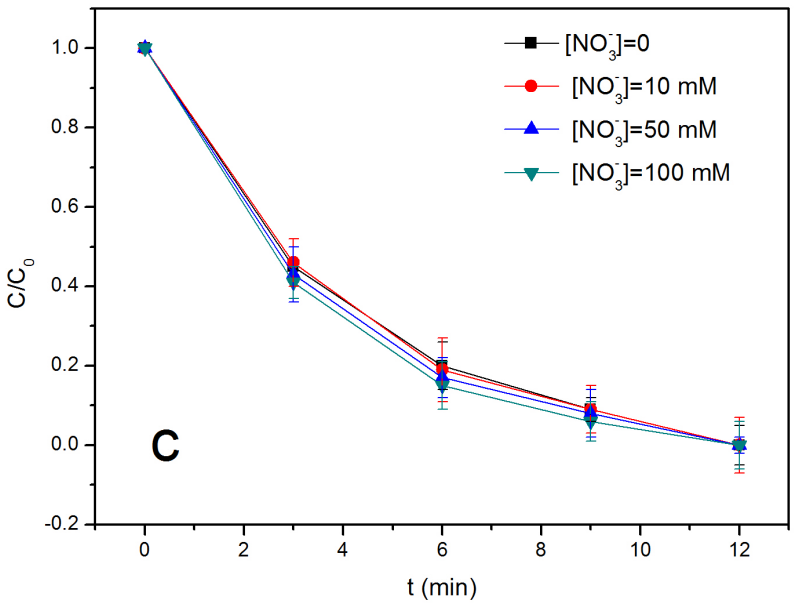
[NO3-]=0
[NO3-]=10 mM
[NO3-]=50 mM
[NO3-]=100 mM
C/C0
t (min)
c

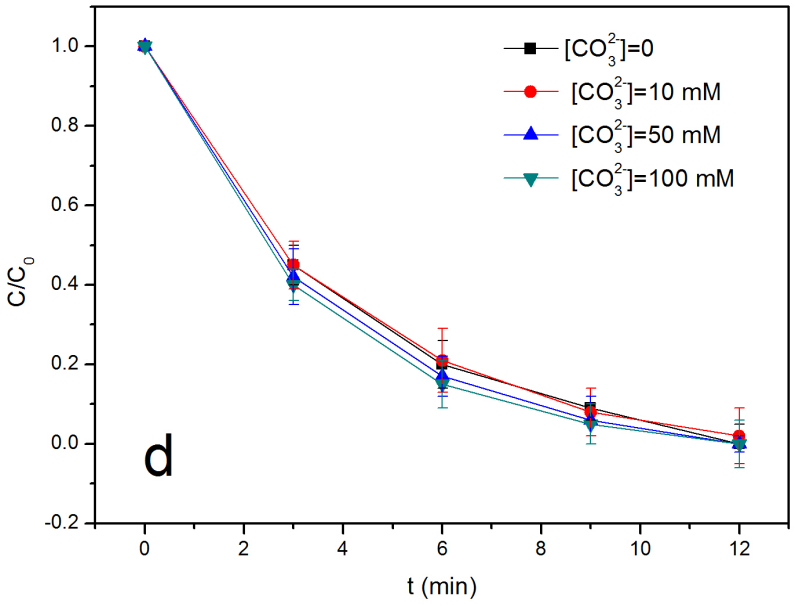
[CO32-]=0
[CO32-]=10 mM
[CO32-]=50 mM
[CO32-]=100 mM
C/C0
t (min)
d

Fig. 5

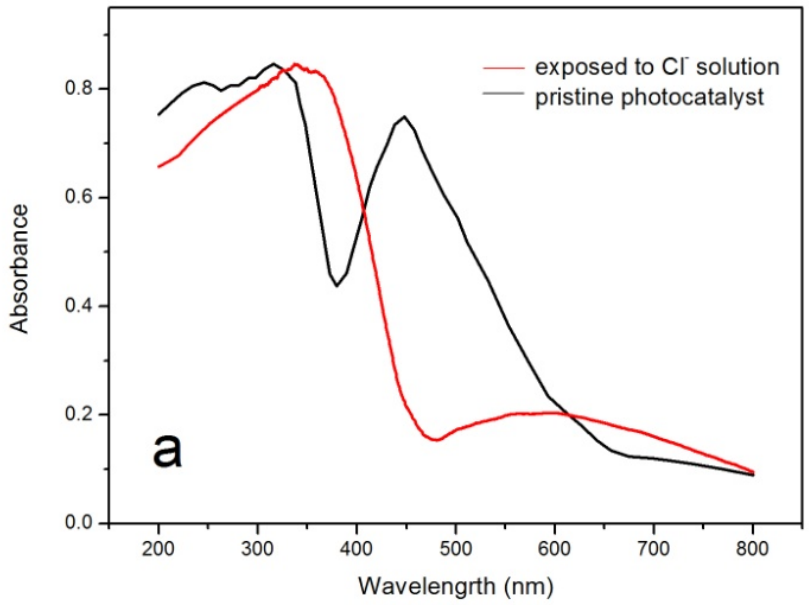
exposed to Cl⁻ solution
pristine photocatalyst
Absorbance
Wavelengrth (nm)
a
0.0
0.2
0.4
0.6
0.8
200
300
400
500
600
700
800

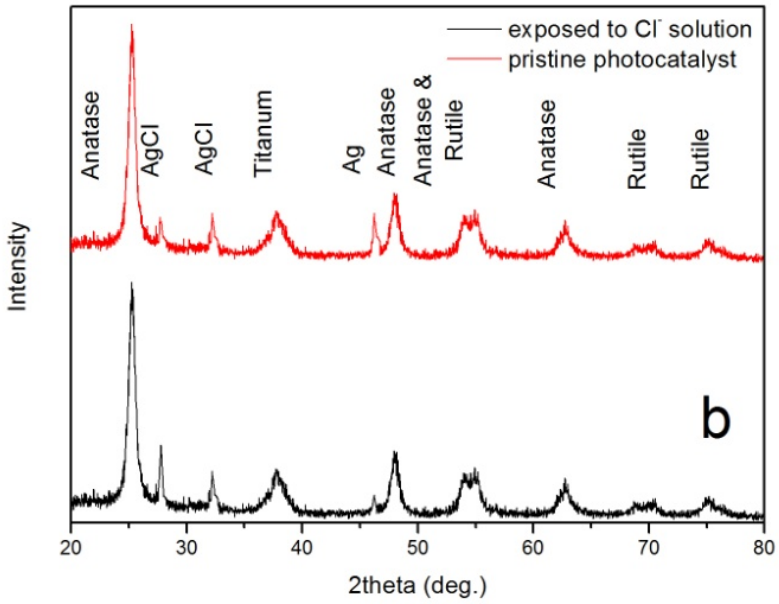
exposed to Cl⁻ solution
pristine photocatalyst
Anatase
AgCl
AgCl
Titanum
Ag
Anatase
Anatase &
Rutile
Anatase
Rutile
Rutile
Intensity
2theta (deg.)
b
20
30
40
50
60
70
80

Fig. 6.

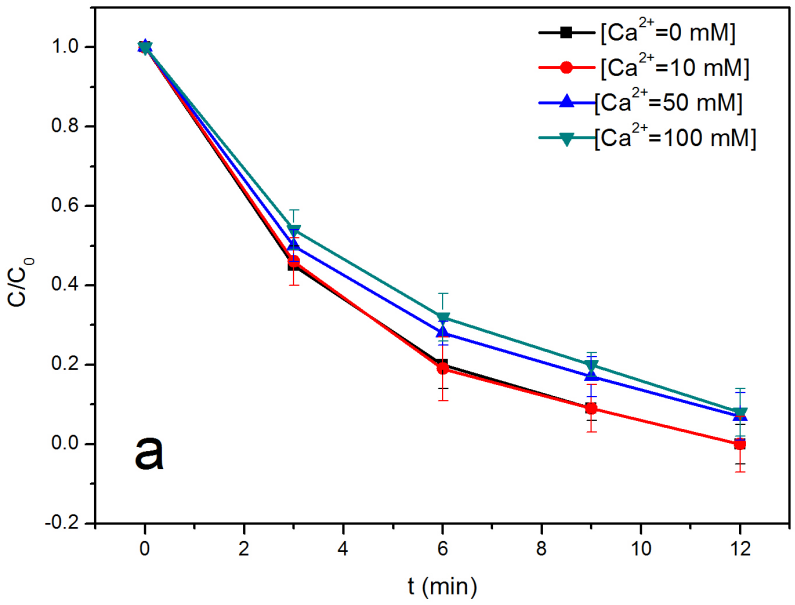

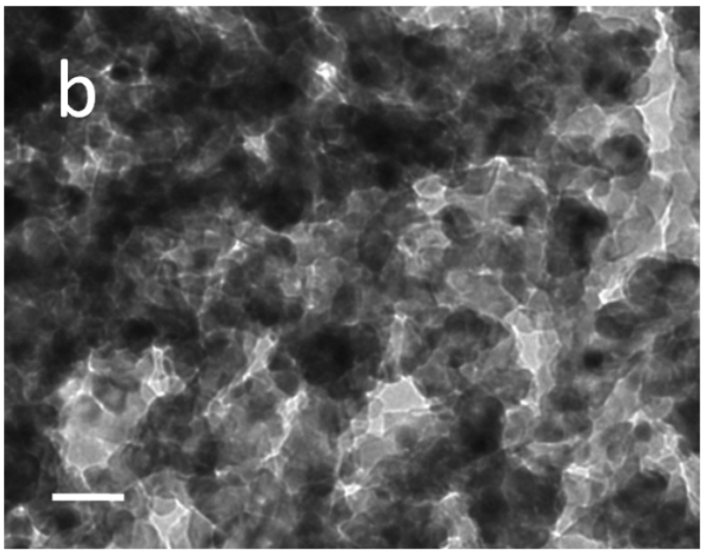

Fig. 7.

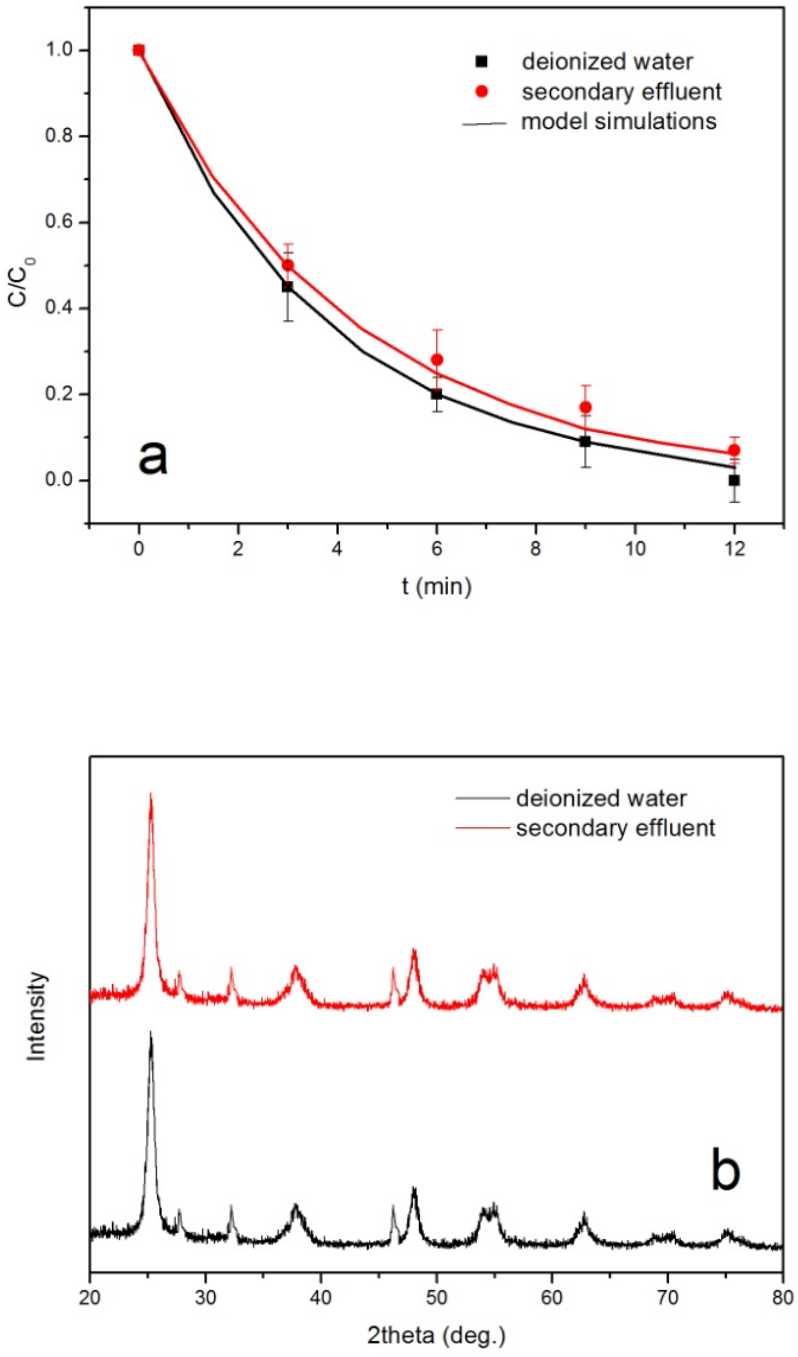
deionized water
secondary effluent
model simulations
C/C0
t (min)
a
deionized water
secondary effluent
Intensity
2theta (deg.)
b

Experimental and mechanism study on the photocatalytic performance of Ag/AgCl @ chiral TiO_2 nanofibers: impact of wastewater components

Dawei Wang [a], Yi Li[a]*, Gianluca Li Puma[b], Chao Wang [a], Peifang Wang [a], Wenlong Zhang [a] and Qing Wang [a]

[a] *Key Laboratory of Integrated Regulation and Resource Development of Shallow Lakes, Ministry of Education, College of Environment, Hohai University. Xi Kang Road #1, Nanjing 210098, PR China; E-mail: envly@hhu.edu.cn*

[b] *Environmental Nanocatalysis & Photoreaction Engineering, Department of Chemical Engineering, Loughborough University, Loughborough LE11 3TU, United Kingdom.*

Table S1. Bulk and surface composition of Ag/AgCl@TiO_2 obtained under different photoreduction time.

Photoreduction time	Ag/Cl molar ratio[a]	Ag^0/Ag^+ [b]	Ag content (wt%)[b]
40	1.92	0.93	9.6
60	2.32	1.28	9.5
80	2.59	1.63	9.5
100	2.92	1.89	9.4

[a] Data from EDS; [b] data from atom absorption spectroscopy (AAS).

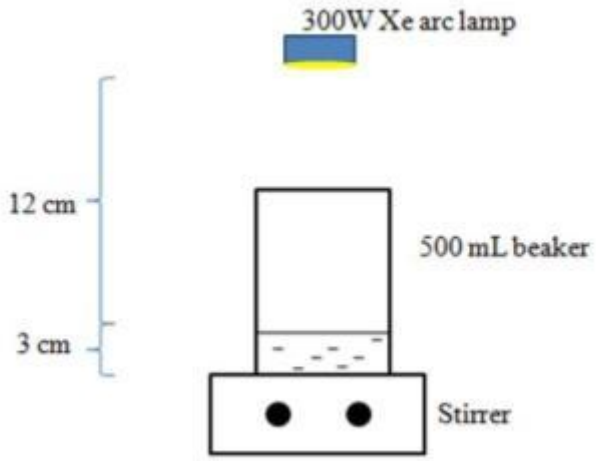

Fig. S1. The reactor of the photocatalytic degradation experiments, the inset picture is the emission spectrum of 300W Xe arc lamp (Philips) with a UV cut-off 25 filter (providing visible light $\lambda \geq 400$ nm).

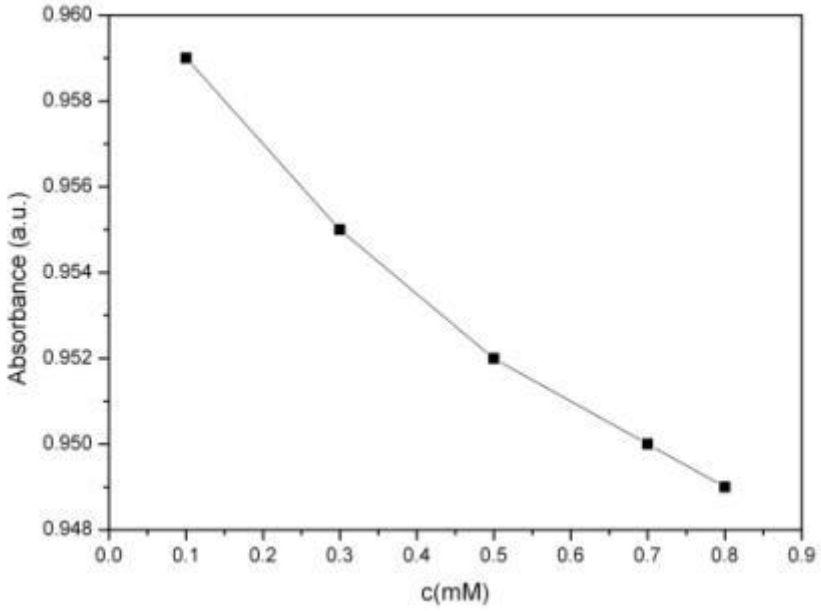

Fig. S2. The relationship between $A_f(CO_3^{\cdot-})_{[EE2]=0} / A_f(CO_3^{\cdot-})$ and C

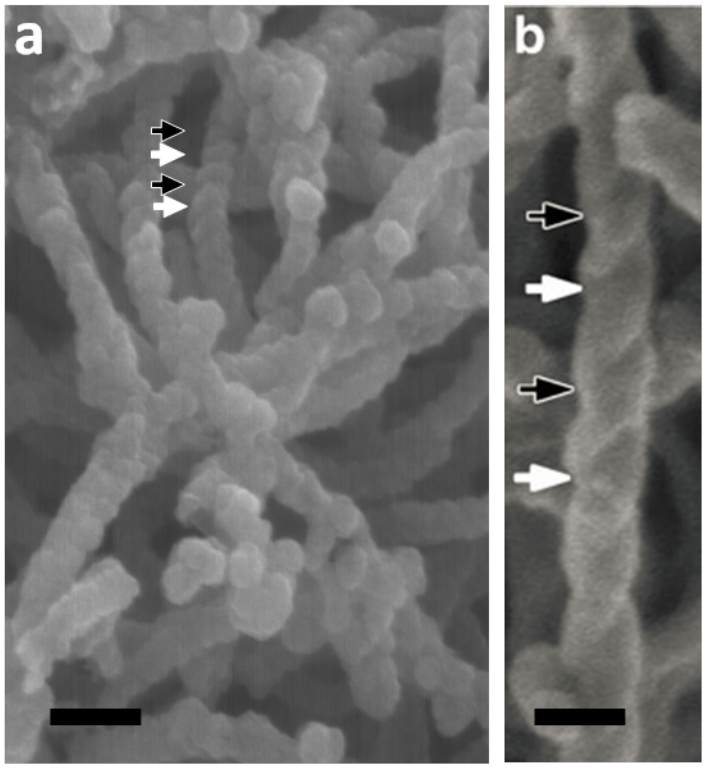

Fig. S3. SEM images of chiral TiO_2 nanofibers. Scale bars in (a) and (b) represent 100 and 50 nm, respectively.

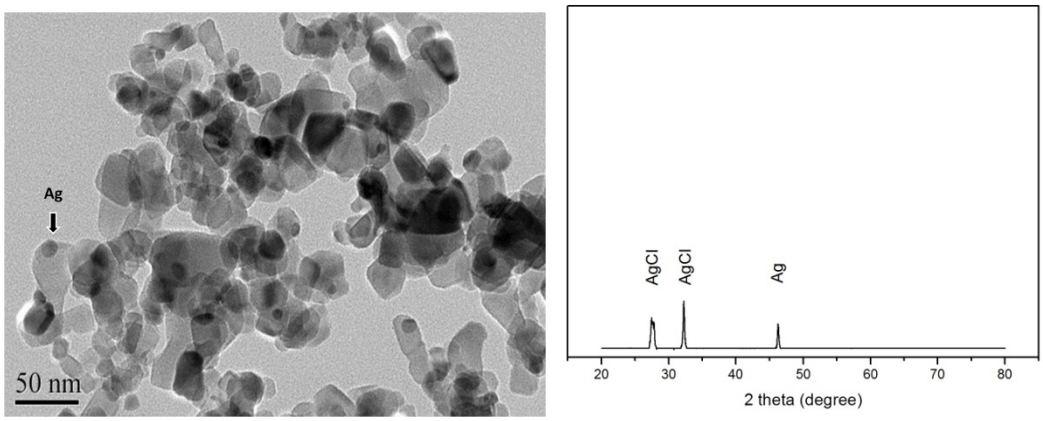

Fig. S4. TEM (left) and XRD (right) of synthesized Ag/AgCl nanoparticles.

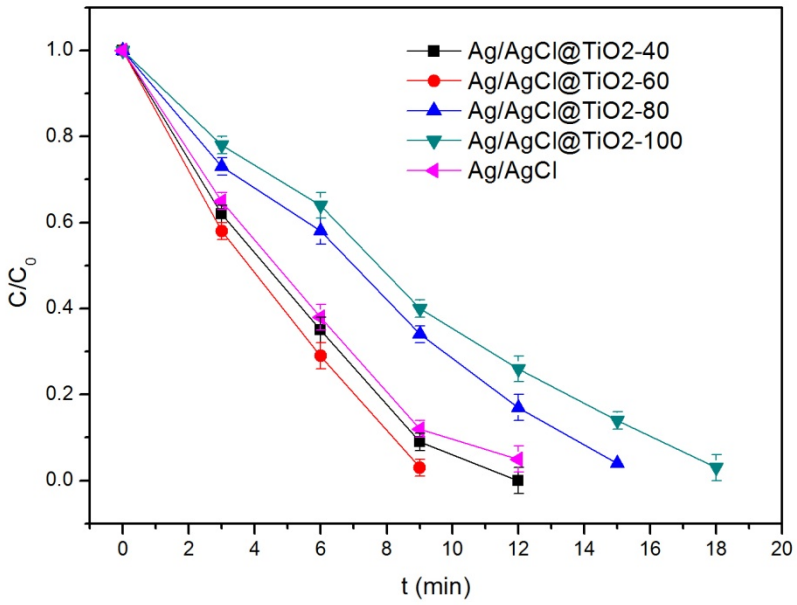

Fig. S5. Photocatalytic performances of Ag/AgCl @ chiral TiO_2 nanofibers obtained under different photoreduction time (40, 60, 80 and 100 min) and Ag/AgCl nanoparticles. The Ag contents clearly had effects on the photocatalytic ability and an optimum ratio can be expected. Among all the tested photocatalysts, Ag/AgCl @TiO_2-60 exhibited the most excellent photocatalytic ability and removed EE2 within about 9 min. Ag/AgCl also showed an excellent photocatalytic performance which is quite close to that of Ag/AgCl@TiO_2-40, but lower than that of Ag/AgCl@TiO_2-60. These results may prove the acceleration effect of chiral TiO_2 on the SPR excitation of Ag to some extent. However, it should also be noted that this comparison may go against control variate method as the sizes, crystalline and contents could be different for Ag/AgCl@ chiral TiO_2 nanofibers and Ag/AgCl nanoparticles.

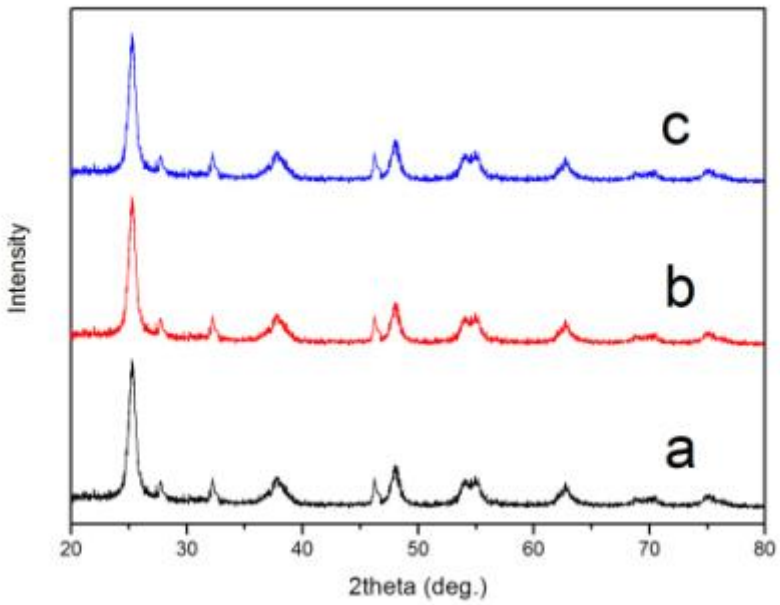

Fig. S6. The effect of (**a**) SO_4^{2-}, (**b**) CO_3^{2-} and (**c**) NO_3^- on the photocatalytic degradation of EE2 using Ag/AgCl @ chiral TiO_2 nanofibers.

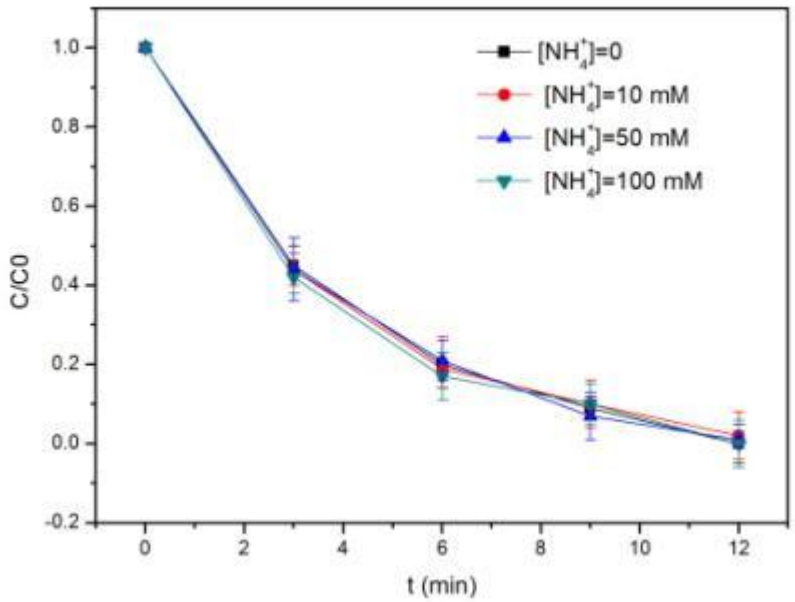

Fig. S7. The effect of NH_4^+ on the photocatalytic degradation of EE2 using Ag/AgCl @ chiral TiO_2 nanofibers.

Relative kinetic rate constants assessment

After the assessment of rate constant for the reaction between Ag/AgCl @ chiral TiO_2 nanofibers, SO_4^{2-} was added into the suspension of TiO_2, EE2, carbonate and distilled water to estimate the second-order rate constant of reaction between SO_4^{2-} and ·OH:

$$Ag/AgCl@chiralTiO_2 \xrightarrow{light} \cdot OH \quad k_0 = 5.2\times10^{10}\,M^{-1}s^{-1} \qquad (S1)$$

$$\cdot OH + CO_3^{2-} \rightarrow CO_3^{\cdot-} + OH^- \quad k_1 = 3.7\times10^{8}\,M^{-1}s^{-1} \qquad (S2)$$

$$\cdot OH + HCO_3^- \rightarrow CO_3^{\cdot-} + H_2O \quad k_2 = 8.5\times10^{6}\,M^{-1}s^{-1} \qquad (S3)$$

$$\left.\begin{array}{l} SO_4^{2-} \xrightarrow{h\nu} productA + \cdot OH \\ SO_4^{2-} + \cdot OH \xrightarrow{h\nu} productA' \end{array}\right\} \; k_4 \qquad (S4)$$

$$EE2 + \cdot OH \rightarrow CO_2 + H_2O \quad k_3 = 9.8\times10^{9}\,M^{-1}s^{-1} \qquad (S5)$$

Similarly, the rate law expression of ·OH was:

$$\frac{d[\cdot OH]}{dt} = k_0[Ag/AgCl@chiralTiO_2] - (k_1[CO_3^{2-}] + k_2[HCO_3^-] + k_3[EE2] + k_4[SO_4^{2-}])[\cdot OH] \qquad (S6)$$

It is noteworthy that SO_4^{2-} accelerates the production of ·OH if $k_4>0$, it inhibits the production if $k_4<0$. Through the same derivation as above, equation (36) was obtained:

$$\frac{A_f(CO_3^{\cdot-})_{[HA]=0}}{A_{f1}(CO_3^{\cdot-})} = 1 + \frac{k_4[SO_4^{2-}]}{k_1[CO_3^{2-}] + k_2[HCO_3^-] + k_3[EE2] - k_0[Ag/AgCl@chiralTiO_2]} \qquad (S7)$$

And k_4 was determined to be $3.9\times10^{5}\,M^{-1}s^{-1}$. Through the similar derivation (details not shown), all second-order rate constants for the reactions between water components and ·OH were obtained.